Available online at www.sciencedirect.com
ScienceDirect
Journal of Magnesium and Alloys xxx (xxxx) xxx
www.elsevier.com/locate/jma

Full Length Article

In situ TEM observations and molecular dynamics simulations of deformation defect activities in Mg via nanoindentation

Yi-Cheng Lai[a,1], Yubin Ying[b,1], Digvijay Yadav[a], Jose Guerrero[a], Yong-Jie Hu[b,*], Kelvin Y. Xie[a,*]

[a] *Department of Materials Science and Engineering, Texas A&M University, College Station, TX 77845, USA*
[b] *Department of Materials Science and Engineering, Drexel University, Philadelphia, PA 19104, USA*

Received 15 December 2022; received in revised form 28 July 2023; accepted 15 August 2023
Available online xxx

Abstract

In this work, we performed *in situ* nanoindentation in TEM to capture the real-time $\langle \boldsymbol{c} + \boldsymbol{a} \rangle$ dislocation and twinning activities in pure Mg during loading and unloading. We demonstrated that the screw component of $\langle \boldsymbol{c} + \boldsymbol{a} \rangle$ dislocations glides continuously, while the edge components rapidly become sessile during loading. The twin tip propagation is intermittent, whereas the twin boundary migration is more continuous. During unloading, we observed the elastic strain relaxation causes both $\langle \boldsymbol{c} + \boldsymbol{a} \rangle$ dislocation retraction and detwinning. Moreover, we note that the plastic zone comprised of $\langle \boldsymbol{c} + \boldsymbol{a} \rangle$ dislocations in Mg is well-defined, which contrasts with the diffused plastic zones observed in face-centered cubic metals under the nanoindentation impressions. Additionally, molecular dynamics simulations were performed to study the formation and evolution of deformation-induced crystallographic defects at the early stages of indentation. We observed that, in addition to $\langle \boldsymbol{a} \rangle$ dislocations, the I_1 stacking fault bounded with a $\langle 1/2\boldsymbol{c}+\boldsymbol{p} \rangle$ Frank loop can be generated from the plastic zone ahead of the indenter, and potentially serve as a nucleation source for abundant $\langle \boldsymbol{c} + \boldsymbol{a} \rangle$ dislocations observed experimentally. These new findings are anticipated to provide new knowledge on the deformation mechanisms of Mg, which are difficult to obtain through conventional *ex situ* approaches. These observations may serve as a baseline for simulation work that investigate the dynamics of $\langle \boldsymbol{c} + \boldsymbol{a} \rangle$ dislocation slip and twinning in Mg and alloys.

Keywords: *In situ* TEM; Molecular dynamics simulation; Dislocation; Twinning; Mg; Nanoindentation.

---

1. Introduction

Magnesium and its alloys have received considerable interest because of their relatively high strength-to-weight ratio, making them promising structural materials for automotive and aerospace applications [1–3]. However, its limited ductility and formability, which stems from the plastic anisotropy due to its hexagonal-close-packed (HCP) crystal structure [4], limits its wider uses. There are two main deformation mechanisms for Mg – slip and twinning [5–8].

Among all deformation mechanisms, the $\langle \boldsymbol{c} + \boldsymbol{a} \rangle$ pyramidal slip and extension twinning are of particular interest. The $\langle \boldsymbol{c} + \boldsymbol{a} \rangle$ slip is the only dislocation slip mechanism that can accommodate the ***c***-axis compression. The critical resolved shear stress for $\langle \boldsymbol{c} + \boldsymbol{a} \rangle$ is approximately 50 MPa, 100 times higher than that of the basal $\langle \boldsymbol{a} \rangle$ slip [5]. The $\langle \boldsymbol{c} + \boldsymbol{a} \rangle$ dislocation has Burgers vector$\{11\bar{2}3\}$, and can glide on $\{10\bar{1}1\}$ pyramidal I planes and $\{11\bar{2}2\}$ pyramidal II planes [7,9–11]. Wu and Curtin pointed out that $\langle \boldsymbol{c} + \boldsymbol{a} \rangle$ dislocation can undergo thermally-activated pyramidal-to-basal core transition, rendering them sessile and no longer to accommodate the ***c***-axis compression [12,13]. Hence, understanding the characteristics of $\langle \boldsymbol{c} + \boldsymbol{a} \rangle$ dislocations and subsequently tailoring their slip behavior (e.g., via alloying) is critical to achieving Mg alloys with improved ductility and formability

---

[*] Corresponding authors.
E-mail addresses: yh593@drexel.edu (Y.-J. Hu), kelvin_xie@tamu.edu (K.Y. Xie).

[1] These authors contributed equally to this work.

https://doi.org/10.1016/j.jma.2023.08.013

Please cite this article as: Y.-C. Lai, Y. Ying, D. Yadav et al., In situ TEM observations and molecular dynamics simulations of deformation defect activities in Mg via nanoindentation, Journal of Magnesium and Alloys, https://doi.org/10.1016/j.jma.2023.08.013

[8–10,12–20]. The $\langle 10\bar{1}1\rangle$ $\{10\bar{1}2\}$ extension twinning is the only mechanism that can accommodate $\boldsymbol{c}$-axis tension [6]. Compared to $\langle \boldsymbol{c}+\boldsymbol{a}\rangle$ slip, extension twinning is much easier to activate, with only approximately 5 MPa critical resolved twin stress [5]. Therefore, they are commonly observed in Mg samples pulled along the $\boldsymbol{c}$-axis or compressed perpendicular to the $\boldsymbol{c}$-axis [6,21–24]. Once nucleated and the twin tip has propagated, the twin boundary can migrate either via twinning shear or atomic shuffling, leading to twin thickening [25–28].

We note that a large body of characterization work on $\langle \boldsymbol{c}+\boldsymbol{a}\rangle$ dislocations and extension twins are *postmortem*, which may result in two drawbacks. First, only the end results can be captured, and the microstructural evolution is lost. Second, most elastic strain is relaxed. The dislocation and twin structures may have changed during unloading, thus affecting the result interpretation. *In situ* imaging using transmission electron microscopy (TEM) combined with mechanical tests can overcome the above challenges [29–40]. *In situ* TEM allows for the direct observation of microstructural evolution during deformation as well as during unloading. For example, Liu et al. performed nanopillar compression to study the $\langle \boldsymbol{c}+\boldsymbol{a}\rangle$ dislocation slip [40] and extension twin boundary migration [28,41]. However, nanopillars generally exhibit a high surface-to-volume ratio; dislocations tend to escape to the surface. Moreover, the small volumes of nanopillars cannot contain an entire twin. In this work, we adopted the “H-bar” design and nanoindentation experiment described by Zhang et al. [37] that offers enough volume for extensive dislocation activities and to capture the twin nucleation, twin tip propagation, and twin boundary migration events, together with the load-displacement information.

As a complementary method to the *in situ* experiments, we also carried out molecular dynamics (MD) simulations to provide a deeper understanding of crystallographic defect generation and deformation mechanisms activated during nanoindentation at an atomistic scale. By simulating the dynamic process of the interactions between a nanosized indenter and an Mg bulk substrate, the MD simulations can detail the formation and evolution of crystallographic defects during the very early stages of indentation to provide an atomistic interpretation of the dislocation and twining activities observed experimentally.

2. Materials and methods

2.1. Experimental setup

A well-annealed hot-rolled commercially pure Mg was used for this study. The detailed processing conditions and microstructural information can be found in our previous work [42]. Half discs of 3 mm in diameter and 120 µm in thickness were prepared, then electropolished using a twin-jet electropolisher (TenuPol-5, Struers) using 10% nitric acid at −35 °C to reduce the flat-edge thickness to approximately 5 µm. A focused ion beam (FIB, Helios G4, ThermoFisher, 30 kV Ga^+ beam at the 0.2 nA current) was used to create 5 µm wide and 500 nm thick windows on the flat edge of the half-discs, which are to be indented. Due to the low atomic number of Mg, 500 nm thick windows are still electron transparent when imaged using transmission electron microscopy (TEM). Having relatively thick windows (500 nm) is advantageous compared to thinner ones (e.g., ~100 nm). First, the surface effect will be less prominent in the thick foils, the microstructural evolution of which resembles more of that in bulk samples. Second, there will be less foil bending during *in situ* indentation for thicker foils, as specimen bending can give rise to unwanted artifacts such as bending contours. The TEM characterizations were performed in an FEI Tecnai TEM operated at 200 keV and equipped with a NanoMEGAS ASTAR system for precession electron diffraction (PED) experiments. The precession angle was 0.3° and the step size was 7 nm when acquiring the map.

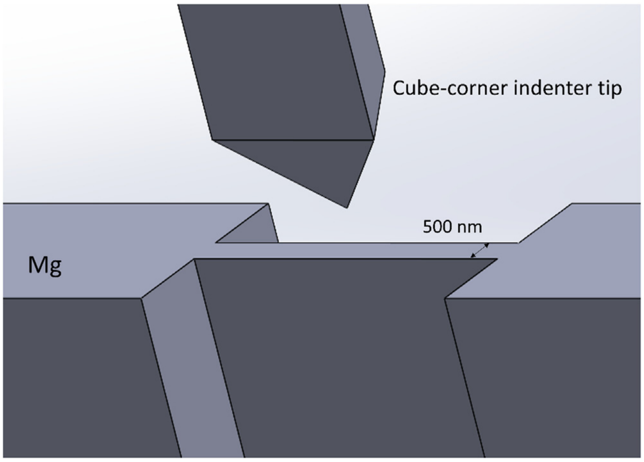

Fig. 1. A schematic of the *in situ* nanoindentation setup in this work.

The *in situ* nanoindentation was carried out using a PI95 TEM PicoIndenter equipped with a three-sided cube-corner tip. Indentation experiments were performed at a rate of 5 nm s^{-1}. The schematic of the *in situ* indentation setup is shown in Fig. 1. Imaging and video recording were carried out with an FEI Tecnai TEM operating at 200 kV. In the results shown in this work, the $\boldsymbol{g}$-vector of [0002] was used. This condition reveals the $<\boldsymbol{c}>$-component of $\langle \boldsymbol{c}+\boldsymbol{a}\rangle$ dislocations and renders $\langle \boldsymbol{a}\rangle$ dislocations and $<\boldsymbol{a}>$-component of $\langle \boldsymbol{c}+\boldsymbol{a}\rangle$ dislocations invisible [7,20]. Hence, the dislocation activities revealed in this work are those of $\langle \boldsymbol{c}+\boldsymbol{a}\rangle$ dislocations.

2.2. MD simulations setup

The molecular dynamic (MD) simulations of nanoindentation were performed using the open-access Large-scale atomic/molecular massively parallel simulator (LAMMPS) package [43]. A well-accepted embedded-atom-method (EAM) potential developed by Sun et al. was employed to describe the interatomic force field and potential energy in the MD simulations [44]. An orthorhombic simulation cell with periodic boundary conditions was used for the nanoindentation simulation. As schematically illustrated in Fig. 2, a

Please cite this article as: Y.-C. Lai, Y. Ying, D. Yadav et al., In situ TEM observations and molecular dynamics simulations of deformation defect activities in Mg via nanoindentation, Journal of Magnesium and Alloys, https://doi.org/10.1016/j.jma.2023.08.013

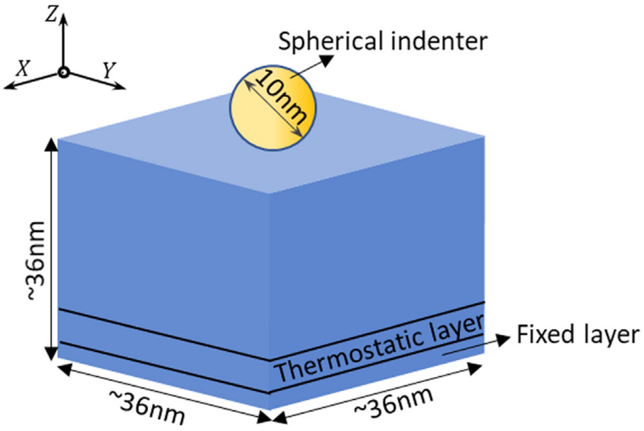

Fig. 2. Schematic diagram of the MD simulation model for the nanoindentation.

bulk substrate of perfect HCP Mg was enclosed in the simulation cell to fill both the x and y directions and expose free surfaces along the z direction to interact with the indenter. The indentation behaviors of two different surfaces were simulated. One was the tension twining plane $(10\bar{1}2)$, which has a crystallographic orientation close to the loading surface of the experimental indentation. The other surface was the second-order prismatic slip plane $(1\bar{2}10)$. Because the loading conditions in the experimental indention test may not be as ideal as the MD simulation, we took the simulation of the prismatic plane as a validation to confirm the deformation phenomena observed in the twining plane simulation are relatively general and not sensitive to the orientation setup of the indention surface. The bulk substrate contains about 2 million atoms and has a size of about 36 nm × 36 nm × 36 nm along the x, y, and z directions, respectively. The exact sizing values vary slightly depending on the crystal orientation of the substrate. Before the indention, the substrate was equilibrated at 300 K for 100 ps with the isothermal-isobaric ensemble (NPT).

As shown in Fig. 2, a non-atomistic spherical indenter with a diameter of 10 nm was positioned above the center of the substrate to have its edge just touching the substrate surface. Although a cube-cornered tip was used in the experiment, there is always tip rounding at the apex and the initial contact is Hertzian. Hence, a spherical indenter tip was constructed for the MD simulations. The indenter was represented to be non-atomistic because only atomic displacement in the substrate is of interest. To simulate the loading force and deformation induced by indention, the indenter exerted a repulsive force $F(r)$ to the atoms in the substrate with a magnitude of

$$F(r) = \begin{cases} -K(r-R)^2, & r \le R \\ 0, & r > R \end{cases} \tag{1}$$

where K is the stiffness constant of the indenter and was set to be 10 eV/A^3 , much stiffer than that of pure HCP Mg. R is the indenter radius, and r is distance from the substrate atom to the center of the indenter. The indentation process was then simulated by moving the indenter toward the Mg substrate at a constant velocity. To reduce the “artificial effect” of the unavoidable high-strain-rate setup of MD simulations, the indenter was moved in a “run-and-hold” mode. Specifically, the indenter was moved at a constant velocity of 10 m/s for 20 ps and then hold at the position for another 20 ps. As such, we expected the system would be able to be sufficiently relaxed at the holding period to allow for the nucleation and evolvement of deformation defects that may be prohibited by the high-strain-rate deformation. The “run-and-hold” process was iteratively repeated until the indentation depth reached 2 nm. Subsequently, we increased the loading period to 100 ps to achieve a final indentation depth of 3 nm. Following this, we maintained the indenter position for an additional 200 ps to ensure an adequate development of the plastic zone, as well as the emission and evolution of dislocations. As shown in Fig. 2, during the indentation, the last 4 layers of atoms at the bottom of the substrate were fixed. Above the fixed layers, another 8 layers of atoms were assigned as a thermostatic region to dissipate the joule heat generated by indentation deformation in a limited simulation volume [45]. The temperature of the atoms in the thermostatic region was rescaled to 300 K at each MD timestep. After the indenter reached 3 nm, it was held at the position for 600 ps at 300 K using the canonical (NVT) ensemble to equilibrate the atomic structure of the indented substrate.

The atomic structure of the substrate was recorded at different timesteps to evaluate the nucleation and evolvement of deformation defects during the indentation process. For each structural snapshot, a static conjugate gradient minimization was applied to eliminate thermal fluctuations. The OVITO software was used for visualization, and the common neighbor analysis (CNA) and dislocation analysis (DXA) embedded in OVITO were used to analyze the atomistic structure of the deformation defects generated during the indentation [46].

Additionally, for better understanding the dislocation reaction phenomenon observed in the indentation experiment, we also carried out MD simulations on the glide behavior of a pre-existing, straight screw $\langle c + a \rangle$ dislocation under a loading-unloading shear deformation process. The dislocation was embedded in a bulk crystal with a geometry about 24.3 × 17.8 × 17.3 nm^3, where the x axis is along the direction of Burgers vector, $\vec{b} = 1/3[2\bar{1}\bar{1}3]$, with a length of 20$b$, and the y-z plane parallel to the pyramidal I plane. Periodic boundary condition was applied for both the x and y direction. The initial dislocation structure was generated using the ATOMSK software [47]. After an initial relaxation, a shear strain along the $1/3[2\bar{1}\bar{1}3]$ direction on the pyramidal I plane was applied by assigning a constant velocity to the atoms in the upper 1 nm slab along the z axis of the bulk and keeping the atoms in the bottom 1 nm slab fixed. The overall strain rate was2×10^{-5}ps^{-1}, and the system was equilibrated with an isothermal–isobaric (NPT) ensemble at a temperature of 10 K and zero pressure along the x direction. The shear stress was calculated as$\sigma_{xz} = F_x/A_{xz}$, where F_x is the total force on the upper slab atoms in the x direction and A_{xz} is the area [48]. After yielding, an inverse strain was applied to mimic the relaxation of the remaining elastic strain

Please cite this article as: Y.-C. Lai, Y. Ying, D. Yadav et al., In situ TEM observations and molecular dynamics simulations of deformation defect activities in Mg via nanoindentation, Journal of Magnesium and Alloys, https://doi.org/10.1016/j.jma.2023.08.013

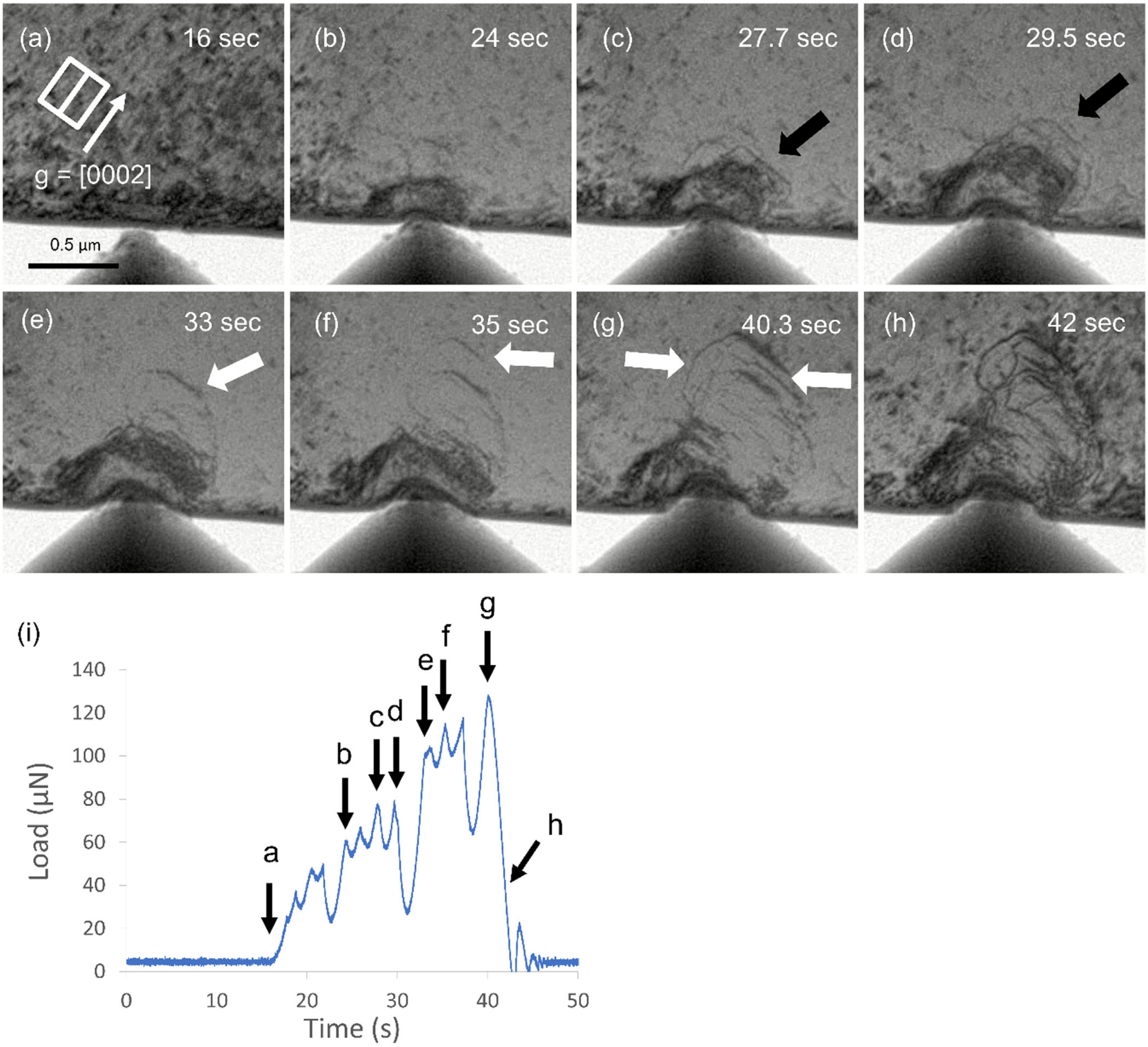

Fig. 3. (a–h) Bright-field TEM images during the first indentation test. (i) The load-time profile obtained by the machine; the arrows indicate where the (a–h) images are taken.

during the unloading process of the indentation experiment. The OVITO software was used for visualization and analysis of atomic structures [46].

3. Results and discussions

3.1. Experimental observations and discussions

The initial deformation behavior of the pure Mg sample and the load-time curve are shown in Fig. 3. The time-series collection of bright-field TEM images (Fig. 3a–h) is the still frames of the *in situ* nanoindentation movie (*Supplementary Information,* S.I. 1) from the first round of the nanoindentation experiment. The corresponding mechanical responses are indicated in the load-time curve in Fig. 3i. The initial distance between the indenter and the substrate was roughly 175 nm. In Fig. 3a, the diamond tip started to contact the specimen surface. The deformation quickly entered the plastic regime, as shown in Fig 3b. A near-hemispherical plastic zone developed and grew as the tip pushed into the sample (Fig. 3b–d). The plastic zone at this stage was near-hemispherical, probably due to the rounding of the cube-cornered tip, giving rise to Hertzian contact [49]. As the indentation proceeded, the plastic zone started to become more asymmetric, with more dislocations multiplied on the right side of the tip (shown by the black arrow in Fig. 3c,d). This is expected because the deformation under the "edges" and "faces" of the cube-corned tip is different [50]. Further deformation activated dislocation

Please cite this article as: Y.-C. Lai, Y. Ying, D. Yadav et al., In situ TEM observations and molecular dynamics simulations of deformation defect activities in Mg via nanoindentation, Journal of Magnesium and Alloys, https://doi.org/10.1016/j.jma.2023.08.013

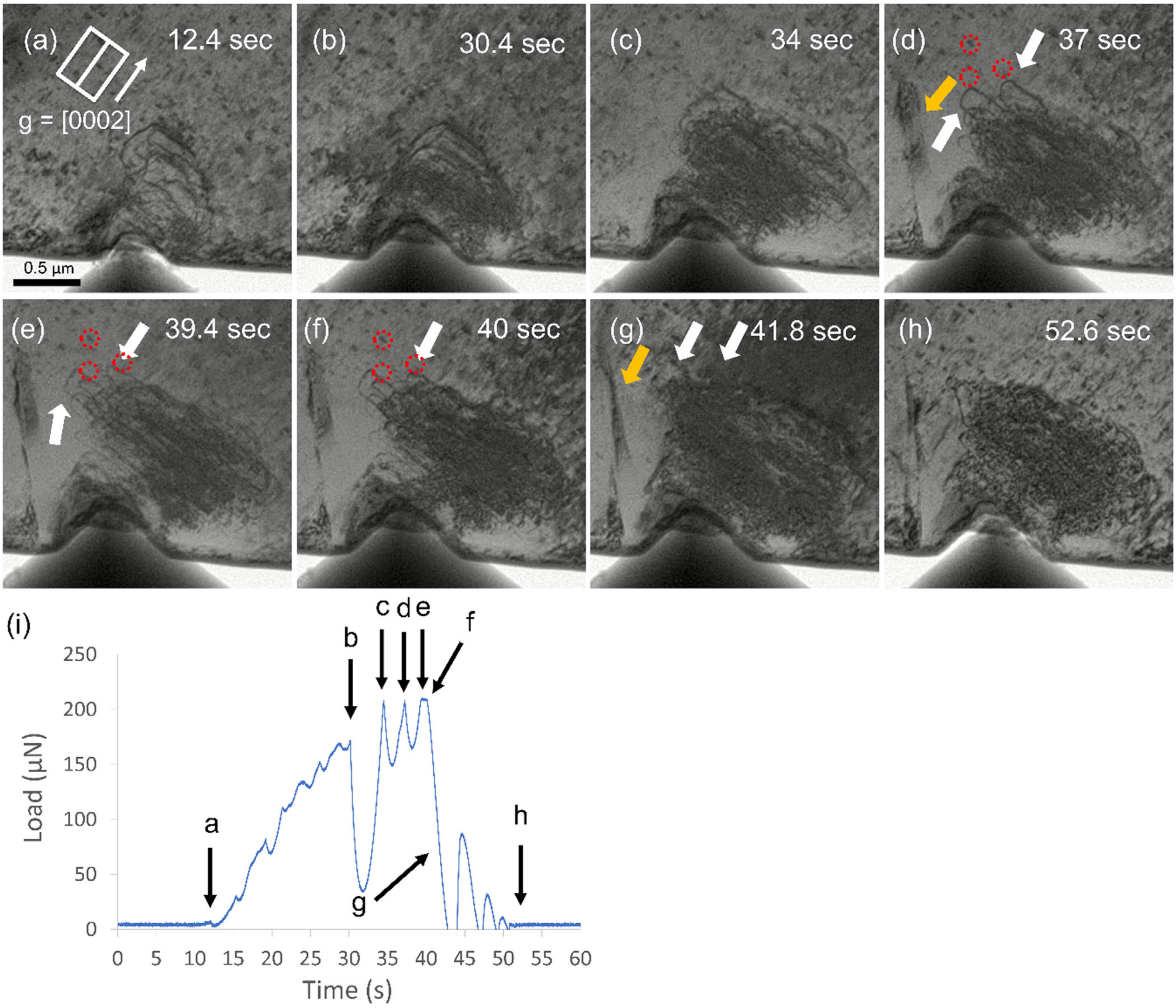

Fig. 4. (a–h) Bright-field TEM images during the second-round indentation test. Three red dotted circles were drawn in d-f as fiducial markers to highlight the relative positions of the dislocations, showing the protruding and retracting behaviors. (i) The load-time profile obtained by the machine; the arrows indicate where the (a–h) images are taken.

nucleation and multiplication outside the well-defined plastic zone, as indicated by the white arrows in Fig. 3e–g. The dislocation density outside the “well-define plastic zone” is low, which allows us to discern individual $\langle \boldsymbol{c} + \boldsymbol{a} \rangle$ dislocation lines. The glide of the edge component (the basal-bound part) is one-time only and tends to rapidly become sessile, whereas the glide of the screw component (the non-basal-bound part) is continuous and remains glissile. The sessile nature of the basal-bound part of the $\langle \boldsymbol{c} + \boldsymbol{a} \rangle$ dislocations is consistent with the molecular dynamics simulations [10,12,51]. It is interesting to note that the overall growth of the plastic zone and the general deformation behavior are not continuous; they are rather intermittent, manifested by strain bursts of different magnitudes [52]. For example, most strain bursts are small, whereas d-to-e is large. The large strain burst is correlated with the sudden massive multiplication of dislocations. In this round of deformation, all strain bursts are associated with dislocation activities, suggesting the stochastic nature of dislocation nucleation and multiplication [53].

To understand the microstructural evolution upon further indentation, we performed second, third, and fourth rounds of indentation in the same area. Fig. 4 shows the deformation behavior (Fig. 4a–h, still frames from movie S.I. 2) and the load-time curve (Fig. 4i) during the second-round indentation. The initial distance between the indenter and the substrate was about 195 nm. In Fig. 4a, the tip came in contact with the specimen. As the indentation proceeded (Fig. 4a–c), the plastic zone grew continuously, and the shape remained asymmetric. With further indentation, in addition to the $\langle \boldsymbol{c} + \boldsymbol{a} \rangle$ dislocation slip (indicated by the white arrows in Fig. 4d–f, consistent with Ref. [37]), a twin also developed in the specimen (indicated by the orange arrow in Fig. 4d). The twin

Please cite this article as: Y.-C. Lai, Y. Ying, D. Yadav et al., In situ TEM observations and molecular dynamics simulations of deformation defect activities in Mg via nanoindentation, Journal of Magnesium and Alloys, https://doi.org/10.1016/j.jma.2023.08.013

appeared suddenly, and the TEM camera (0.5 s per frame) does not have the time resolution to capture its nucleation. The first stable form of the twin is 1.3 µm long and 150 nm thick. The twin boundaries are flat and the twin appears to be faceted. We noticed that the dislocation density on the left side of the indenter tip is low. The activation of the twin on the left side can effectively relax the stored elastic strain and serve as the plasticity carrier. Unloading occurs from Fig. 4e–4h. It is surprising to note that removing the elastic strain during unloading had a noticeable impact on the twin and some dislocations. The twin shrank in size, and the twin boundaries became curved. This information would have been easily neglected if the work were carried out *ex situ*. Moreover, the glissile components of some free-standing $\langle \boldsymbol{c}+\boldsymbol{a}\rangle$ dislocation retracted (an example see Fig. 4e–g). It is also important to note that the dislocations in the plastic zone did not change significantly during unloading, probably due to the dislocation interlocking. Similar to the first-round indentation, numerous strain bursts were observed here as shown in Fig. 4i. The large strain burst (b-to-c) is related to the sudden growth of the plastic zone (Fig. 4b, c). Unfortunately, twin nucleation and growth (Fig. 4d, e) did not result in apparent strain bursts that can be discerned from the regular dislocation activities in the load-time curve (Fig. 4i).

For the third-round indentation, dislocations continued to multiply, and the twin became thicker. The overall microstructural changes do not offer new insight. Thus, we do not discuss it extensively here but provide the video in the *Supplementary Information* (S.I. 3).

In the fourth-round indentation, both dislocations and the twin continue to evolve. The initial distance between the indenter and the substrate was around 90 nm. At this indentation depth, the dislocations in the plastic zone are too dense to reveal detailed information. However, the overall plastic zone was observed to be growing (Fig. 5a–d, still frames from movie S.I. 4). The twin tip propagated deep into the specimen while the twin grew thicker, as indicated by the orange arrows in Fig. 5b–5d. A closer inspection reveals that the twin activity during loading can be described in two stages. In the first stage (Fig. 5a,b), the twin tip and boundary movement are rather sluggish. This is probably because defects generated during detwinning pinched their free movements. In the second stage (Fig. 5c,d), the twin tip propagated into the matrix more freely, accompanied by some twin boundary migration (i.e., twin thickening). During unloading (Fig. 5e–h), similar to the second-round indentation, both dislocation retraction (white arrows) and detwinning (orange arrows) were observed. We noted a large strain burst occurred before d in Fig. 5i, which is also likely to be caused by dislocation activities rather than twinning. To confirm that the twin appeared during the tests, we performed the crystal orientation mapping by precession electron diffraction (PED) in TEM. PED is a technique used to acquire high-resolution information such as crystal orientation or strain. The diffraction patterns acquired from each pixel during the precession of the electron beam in TEM are compared to the simulated diffraction patterns in a database. The misorientation line scan profile shown as an inset below Fig. 5h indicates that the wedge-like thing is a typical extension twin with a roughly 85° misorientation angle with respect to the matrix.

The knowledge generated from this work provides new insight into the deformation behavior of Mg. First, we revealed how $\langle \boldsymbol{c}+\boldsymbol{a}\rangle$ dislocations glide and twins grow in the Mg sample during loading. The screw component of $\langle \boldsymbol{c}+\boldsymbol{a}\rangle$ dislocations glides continuously, while the edge components glide only once at their early stage of dislocation multiplication and then rapidly become sessile. The twin tip propagation is intermittent, whereas the twin boundary migration is more continuous. Second, we demonstrated that unloading (i.e., elastic strain relaxation) causes $\langle \boldsymbol{c}+\boldsymbol{a}\rangle$ dislocation retraction and detwinning. During the $\langle \boldsymbol{c}+\boldsymbol{a}\rangle$ dislocation retraction, the screw components (non-basal-bound part) travel in the reverse direction compared to that upon loading and the edge components (basal-bound part) remain sessile but become shorter. During detwinning, the twin tip only withdrew slightly but the twin thickness substantially reduces. The previously flat twin boundaries also became curved after unloading. Third, we observed detwinning may have generated numerous defects, which hinders further twin growth. Once the twin has overcome those defects, the growth proceeds more easily. This observation is anticipated to offer new information for researchers who research the fatigue behavior of Mg and Mg alloys, in which twinning and detwinning are prevalent. Fourth, we note that the plastic zone comprises of $\langle \boldsymbol{c}+\boldsymbol{a}\rangle$ dislocations in Mg is drastically different from that of face-centered-cubic (FCC) metals. Ma et al. reported the plastic zone under the indent in a Ni sample is diffuse at low indentation depths (e.g., 200 nm) and forms multiple subgrains at high indentation depths (e.g., 800 nm) [54]. On the contrary, the plastic zone consists of $\langle \boldsymbol{c}+\boldsymbol{a}\rangle$ dislocations under the indent in Mg is better defined, which is likely due to their lower mobility, in particular the immobility of the edge components, compared to dislocations in FCC metals. Based on the differences described above, we predict that the indentation size effect of Mg better obeys the Nix-Gao model if the $\langle \boldsymbol{c}+\boldsymbol{a}\rangle$ dislocations are the dominant deformation mechanism [55,56].

3.2. MD simulation observations and discussions

In this work, MD simulations were performed to provide atomistic insights on the deformation and defect generation mechanisms acting during indentation and to understand the origin of $\langle \boldsymbol{c}+\boldsymbol{a}\rangle$ dislocations observed in the *in situ* nanoindentation experiments. We are also aware that the indenter size and indentation depth of the simulation are much smaller than those in the actual experiment. Therefore, we consider the MD simulations essentially an atomistic description of the deformation acting at the very early stage of the experimental indentation.

3.2.1. Formation of prismatic ≤a≥ dislocation half-loop

Fig. 6 illustrates the evolvement of atomic structure for the substrate with the $(10\bar{1}2)$ surface during the indentation

Please cite this article as: Y.-C. Lai, Y. Ying, D. Yadav et al., In situ TEM observations and molecular dynamics simulations of deformation defect activities in Mg via nanoindentation, Journal of Magnesium and Alloys, https://doi.org/10.1016/j.jma.2023.08.013

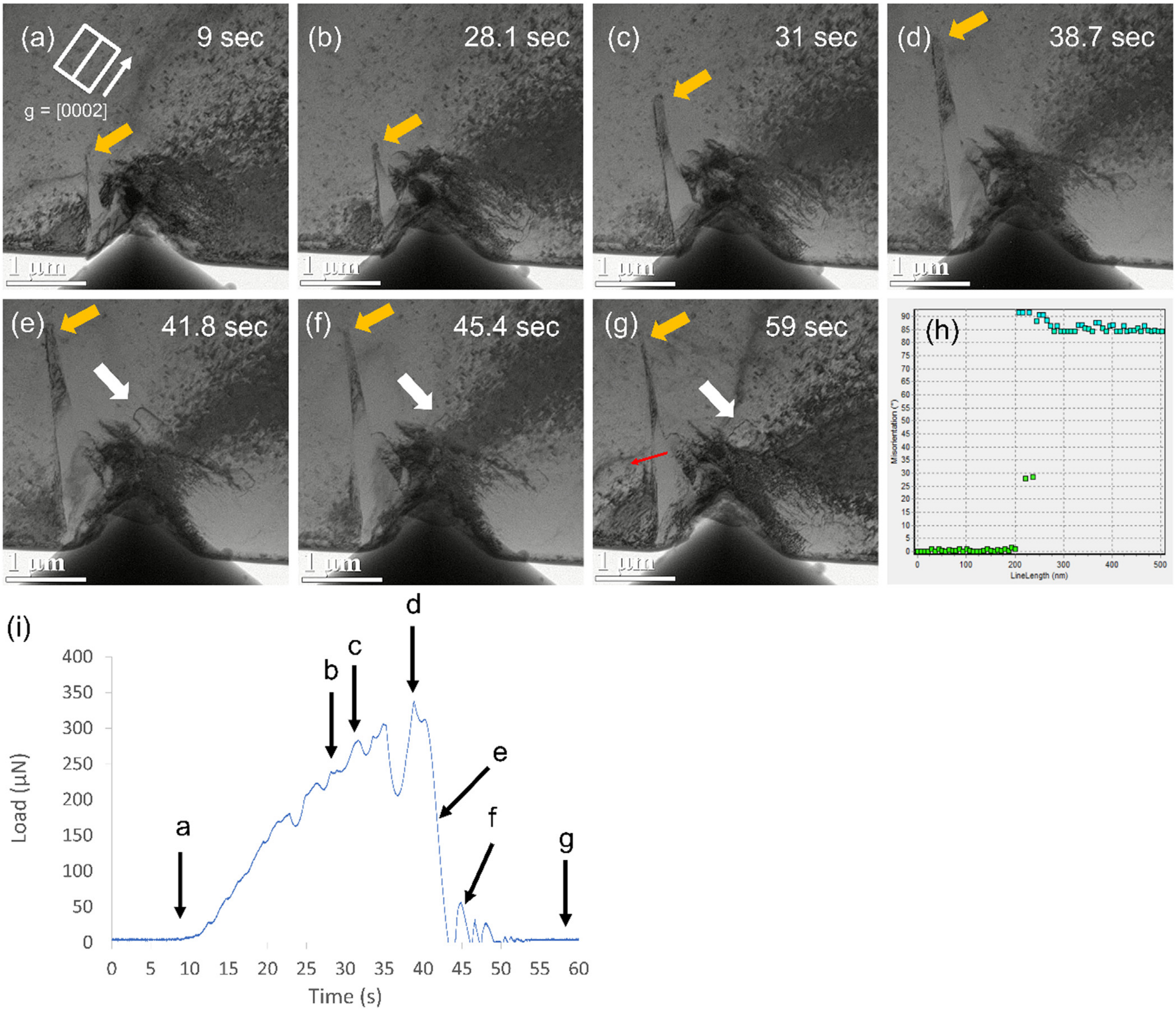

Fig. 5. (a–h) Real-time bright-field TEM images during the fourth round indentation test. The point-to-origin misorientation line scan profile corresponding to the red arrow in (g) is shown in (h). (i) The load-time profile obtained by the machine; the arrows indicate where the (a–h) images are taken.

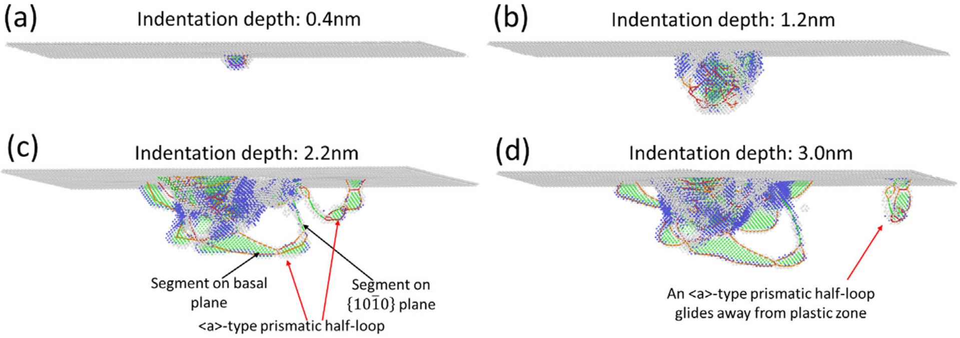

Fig. 6. Atomic structure evaluation for the substrate with the (10$\bar{1}$2) surface during the indentation. (a)-(b) Development of a plastic zone at early stages of indentation. (c), (d) Nucleation and propagation of prismatic $\langle a \rangle$ dislocation half-loops from the plastic zone. According to the adaptive Common neighbor analysis (CNA), atoms colored red, blue, green, and gray are in HCP, BCC, FCC, and other structures, respectively. According to the dislocation analysis (DXA) in OVITO, the dislocation lines corresponding to $<a>$-type full dislocation, $<p>$-type Shockley partial, and other types are colored green, orange, and red, respectively. The atoms in the HCP structure are hidden here.

Please cite this article as: Y.-C. Lai, Y. Ying, D. Yadav et al., In situ TEM observations and molecular dynamics simulations of deformation defect activities in Mg via nanoindentation, Journal of Magnesium and Alloys, https://doi.org/10.1016/j.jma.2023.08.013

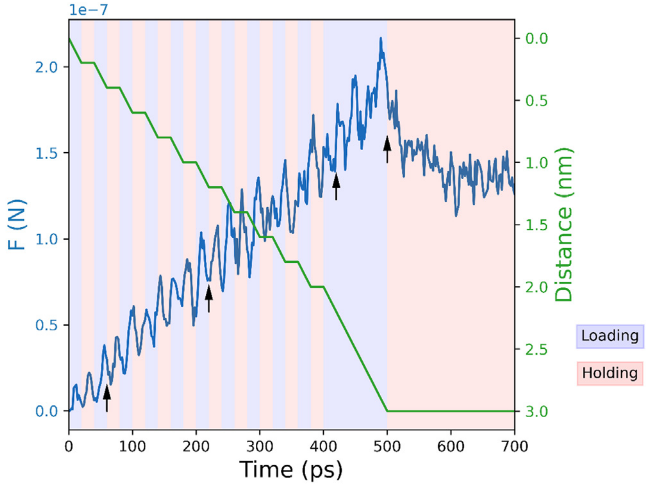

Fig. 7. The load vs. displacement relationship of the indentation simulation with the $(10\bar{1}2)$ surface. The load force and indenter displacement are plotted as a function of time by the blue and green stroke lines, respectively. The time periods corresponding to the loading and holding processes are shaded with lilac and pink colors, respectively. The positions of structural snapshots in Fig. 6 on the loading curve are marked by black arrows.

process. To visualize the deformation defect formation and propagation, only the atoms not in an HCP structure analyzed by the CNA method are shown in Fig. 6. More specifically, the atoms correspond to FCC, body-center cubic (BCC), or other structures are colored in green, blue, and gray, respectively. The respective load-displacement relation of the indentation process is shown in Fig. 7. The positions of the structural snapshots in Fig. 6 on the loading curve are also marked in Fig. 7. As shown in Fig. 6a, a plastic zone is developed at the first stages of indentation. The atoms in the plastic zone are barely in an HCP structure, indicating the local crystal lattice ahead of the intender is severely distorted. As the indention depth increases, the plastic zone grows bigger and tilts along the basal plane due to the activation of multiple dislocations (Fig. 6b). The dislocations are largely entangled and form a network-like structure within the plastic zone, as illustrated by the solid lines in Fig. 6b.

As the indenter penetrates more into the substrate, rather than a continuous growth of the plastic zone, the formation of dislocation loops and stacking faults (SFs) is observed at the surface of the plastic zone. Because of the strain field developed by the indentation, those deformation defects further grow or glide into the matrix to introduce plastic deformation. Among the generated deformation defects, a common one is the prismatic dislocation half-loops with a Burgers vector of $\frac{1}{3}\langle 11\bar{2}0\rangle$ (or $<\boldsymbol{a}>$). The formed half-loops are composed of dislocation segments on either the basal or the first-order prismatic plane. As shown in Fig. 6c, the dislocation segments on the basal plane further dissociate into two $\frac{1}{3}\langle 10\bar{1}0\rangle$ (or $<\boldsymbol{p}>$) Shockley partial dislocations (orange solid lines) and an I_2 stacking fault (two layers of green FCC atoms) with a width of a few atomic distances. In contrast, the dislocation segments on the first-order prismatic plane do not dissociate but are full dislocations with an edge-type character (green solid lines). As illustrated in Fig. 6c,d, the loading from the indenter further drives the half-loops spread into the matrix by the glide of both its basal and prismatic segments, and the contact end of the half-loops can be detached from the plastic zone to the surface of the substrate. The generation of prismatic loops observed here has also been reported in the nanoindentation simulations of Mg and other HCP metals [57]. Similar phenomena are also commonly seen in the FCC and BCC metals [58,59].

3.2.2. Formation of I_1 stacking fault and its implication for ≤c ± a≥ dislocation nucleation

In addition to the prismatic $\langle \boldsymbol{a}\rangle$ half-loops, it is interesting to notice the emergence of the I_1 SFs from the plastic zone during the indentation. An I_1 SF interrupts the basal stacking sequence of an HCP crystal to ABABCBC, where a single layer of atoms at the fault plane experiences aanFCC-like local lattice environment. The formation of the I_1 SFs is of particular interest in the research of Mg because of its intrinsic connection with the activities of $\langle \boldsymbol{c} + \boldsymbol{a}\rangle$ dislocations and alloy ductility [12,60–62]. Particularly, experimental characterization and atomistic simulation suggest that the I_1 SF bounded with a $\langle 1/2\boldsymbol{c}+\boldsymbol{p}\rangle$ Frank loop can serve as an effective nucleation site for the $\langle c + a\rangle$ dislocation and $\{11\bar{2}1\}$ tension twin [61,63,64]. The formation mechanism of I_1 SF in Mg has been mysterious, especially for the “pre-existing” I_1 SFs (i.e., those bounded with a $\langle 1/2\boldsymbol{c}+\boldsymbol{p}\rangle$ Frank loop) that cannot be explained by the edge $\langle \boldsymbol{c} + \boldsymbol{a}\rangle$ dislocation dissociation. A conventional speculation is that the “pre-existing” I_1 results from the condensation of a large number of vacancies or interstitial atoms [65], which can be kinetically difficult to achieve. A recent MD simulation also suggests a new formation mechanism from the defect interactions activated by tension deformation at grain boundaries [66]. Here we show that the I_1 SF bounded with a $\langle 1/2\boldsymbol{c}+\boldsymbol{p}\rangle$ Frank loop can also actively emerge from the deformation process induced by nanoindentation.

Fig. 8a shows the atomic structure of the substrate when the indenter reaches a depth of 3 nm and holds there for 220 ps for equilibration. An I_1 SF formed from the plastic zone is visualized by a single layer of green FCC atoms based on the CNA analysis. We specifically investigate the atomic structure after equilibration to confirm that the observed I_1 formation is not a merely rare event only found in MD simulations with extremely high-strain-rate deformation. To analyze the characteristics of the bounded dislocations of the I_1 SF, we take a projection view of a section of atoms across the SF along the $[2\bar{1}\bar{1}0]$ direction, as marked by the purple box in Fig. 8a. The projected atomic structure is detailed in Fig. 8b, where the atoms are colored by the CNA algorithm. Atoms in the HCP structure are also plotted and colored in red. As shown in Fig. 8b, the fault plane is reflected by a single layer of atoms in green color, which indicates the local lattice environment of the atoms is FCC-like. The gray atoms at the edges of the fault plane correspond to the core structure of the bounded dislocations. It is interesting to also notice that an atomic step forms in the middle of the fault

Please cite this article as: Y.-C. Lai, Y. Ying, D. Yadav et al., In situ TEM observations and molecular dynamics simulations of deformation defect activities in Mg via nanoindentation, Journal of Magnesium and Alloys, https://doi.org/10.1016/j.jma.2023.08.013

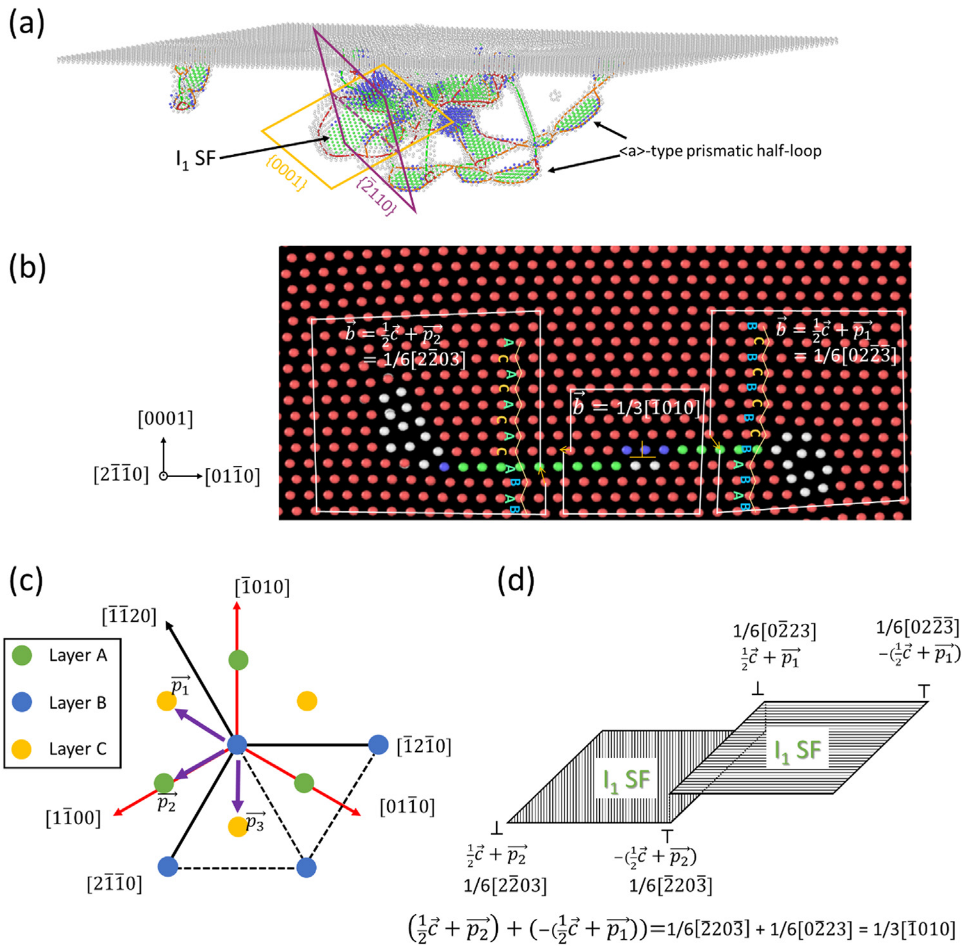

Fig. 8. The detailed atomistic structure of an I_1 stacking fault (SF) formed in the twining plane substrate when holding the indenter at a depth of 3 nm. (a) A snapshot of the atomic structure of the substrate. Only non-HCP atoms are shown. (b) A projected view of the atomic structure of the formed I_1 SF along the [2$\bar{1}\bar{1}$0] direction, as indicated by the purple box in (a). (c) A schematic illustration of the projection view of the atomic sites and vectors on the basal (0001) plane in Mg to support the dislocation analysis in (b). (d) A schematic illustration of the proposed formation mechanism for the I_1 SF observed in (b). The atoms and dislocations are colored in the same mechanism as it in Fig. 6.

plane, at which the fault plane shifts a distance of 1/2<***c***>. The same findings were reported in previous experimental and computational studies [64,67]. Characteristics of the bounded dislocations are scrutinized through Burgers circuit analyses as illustrated in Fig. 3b. The dislocations at the left and right edges of the fault plane are found to be Frank partials with Burgers vectors of 1/6[2$\bar{2}$03] and 1/6[02$\bar{2}\bar{3}$] , respectively. Additionally, a Shockley partial dislocation with a Burgers vector of 1/3[$\bar{1}$010] is found to locate at the edge of the step. Based on the Burgers circuit analyses, a formation mechanism is herein proposed for the observed I_1 SF structure; it results from a dislocation reaction between the Frank partials of two step-free I_1 SFs initially formed on adjacent basal planes. As illustrated by Fig. 8d, one of the I_1 SFs is bounded by the same Frank partial as the left edge of the fault plane observed in Fig. 8b, while the loop dislocation of the other I_1 SF is same as the right edge of the fault plane. As the right edge of the former I_1 contacts the left edge of the latter I_1, the observed Shockley partial can be formed through a dislocation reaction,

$$1/6[\bar{2}20\bar{3}]+1/6[0\bar{2}23]= 1/3[\bar{1}010] \tag{1}$$

Where 1/6[$\bar{2}$203] is the Burgers vector of the Frank partial bounded to the right edge of the former I_1 and 1/6[0$\bar{2}$2$\bar{3}$] is that of the left edge of the latter I_1. Note that for a Frank loop, the dislocations at two facing edges should have Burgers vectors with opposite signs if their line direction is assigned to be the same. Based on a mechanism proposed recently by Agnew et al. [61], both the remaining Frank partials at the edges of the fault plane can serve as nucleation sites to form a ⟨***c*** + ***a***⟩ dislocation half-loop through reactions,

$$1/6[2\bar{2}03] = 1/6[\bar{2}02\bar{3}] + 1/3[2\bar{1}\bar{1}3] \tag{2}$$

and

$$1/6[02\bar{2}\bar{3}] = 1/6[2\bar{2}03] + 1/3[\bar{1}2\bar{1}\bar{3}]$$

Therefore, the MD simulation herein provides a tentative explanation for the abundant activities of ⟨***c*** + ***a***⟩ dislocations observed in the experimental indentation test. That is, I_1 SFs can form at early stages of indentation and serve as an ef-

Please cite this article as: Y.-C. Lai, Y. Ying, D. Yadav et al., In situ TEM observations and molecular dynamics simulations of deformation defect activities in Mg via nanoindentation, Journal of Magnesium and Alloys, https://doi.org/10.1016/j.jma.2023.08.013

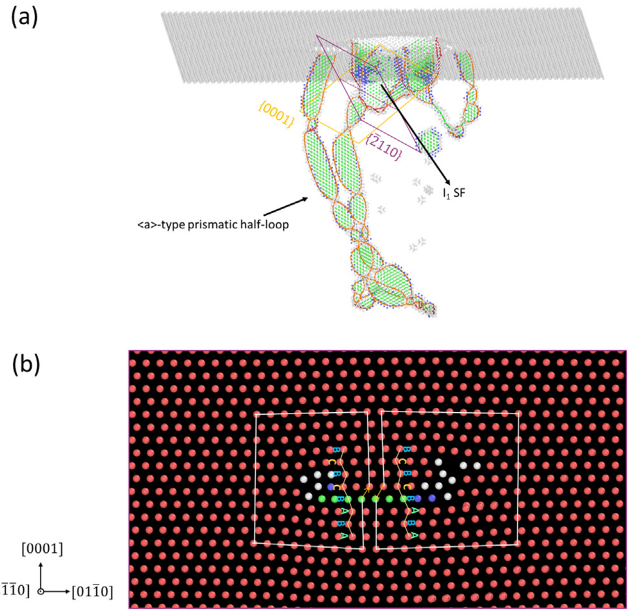

Fig. 9. The detailed atomistic structure of an I_1 stacking fault (SF) formed in the $(1\bar{2}10)$ plane substrate when holding the indenter at a depth of 3 nm. (a) A snapshot of the atomic structure of the substrate. Only non-HCP atoms are shown. (b) A projected view of the atomic structure of the formed I_1 SF along the $[2\bar{1}\bar{1}0]$ direction, as indicated by the purple box in (a). The atoms and dislocations are colored in the same mechanism as it in Fig. 6.

fective source for the nucleating and prorogating of $\langle \boldsymbol{c} + \boldsymbol{a} \rangle$ dislocations.

To confirm the deformation phenomena observed in Figs. 6–8 are not sensitive to the orientation setup of the indentation surface, the same indentation simulation was carried out for the Mg substrate with a $(1\bar{2}10)$ surface. The formation of prismatic $\langle \boldsymbol{a} \rangle$ half-loops and I_1 SFs are both observed, as illustrated by atomic structure analysis shown in Fig. 9. Unlike the I_1 SF observed in twining plane indentation, the I_1 SF formed herein does not have a step in the fault plane and are bounded by Frank partials with opposite Burgers vectors.

3.2.3. Insights for the dislocation retraction during the unloading process

As mentioned in Section 3.1, we observed the retraction of the $\langle c + a \rangle$ dislocation during the unloading process of the experimental indentation. The phenomenon of dislocation retraction is commonly observed in the deformation of metallic materials that possess a high density of twin and/or phase boundaries, such as metallic nanowires [68,69] and nano-lamellar TiAl intermetallic alloys [70,71]. In these materials, the occurrence of dislocation retraction is typically driven by the repulsive image force generated by the interface. A smaller interspacing distance between the interfaces usually leads to a larger image force to promote dislocation retraction [71]. Furthermore, the retraction of dislocations has been found to introduce recoverable plasticity, resulting in a combination of enhanced ductility and strength [68,71].

In contrast to the typical retraction phenomenon observed in nano-lamellar alloys, the retraction of the $\langle c + a \rangle$ dislocation observed our indentation experiment exhibits a limited gliding distance. Given that our material also does not have a nano-lamellar structure, we propose that the observed retraction phenomenon is likely caused by the relaxation of elastic strain and residual stress in the unloading process. We carried out an MD simulation to provide some physical insights for this hypothesis. Because of the intrinsic limitations in the indenter size and the time scale of the MD indentation simulation, we were not able to directly simulate the retraction of the $\langle c + a \rangle$ dislocation during the indentation process. Instead, we simulated the glide behavior of a pre-existing, straight screw $\langle c + a \rangle$ dislocation subjected to a loading-unloading shear deformation process. The details of the simulation setup are described in Section 2.2. In the indentation experiment, the screw segments of the $\langle c + a \rangle$ dislocation

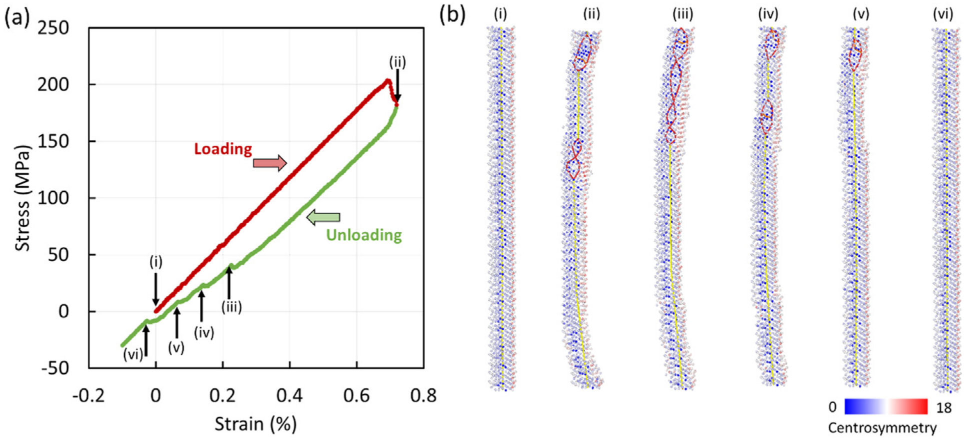

Fig. 10. MD simulation of the glide behavior of a pre-existing screw $\langle c + a \rangle$ dislocation on the pyramidal I plane subjected to a loading-unloading shear deformation process. To replicate practical conditions in indentation experiments, the two ends of the dislocation are artificially pinned. (a) Stress vs. strain curve and (b) atomic structure of the dislocation at different stress-strain conditions. The atoms are color-coded by based on their centrosymmetry parameter values.

Please cite this article as: Y.-C. Lai, Y. Ying, D. Yadav et al., In situ TEM observations and molecular dynamics simulations of deformation defect activities in Mg via nanoindentation, Journal of Magnesium and Alloys, https://doi.org/10.1016/j.jma.2023.08.013

were observed to be mobile and pinned by the sessile edge components. Thereby, in the MD simulation, we artificially introduced pinning points on the pre-existing screw dislocation to qualitatively replicate the experimental condition. A shear strain was applied along the $1/3[2\bar{1}\bar{1}3]$ direction to drive the dislocation gliding on the pyramidal I plane. The stress-strain curve of the deformation process is shown in Fig. 10a. The movements of the dislocation at different stress-strain states are also monitored (Fig. 10b). As shown in Fig. 10, yielding occurs when the applied stress drives the dislocation gliding from its original position to the left. Because of the pining effect, only a part of the dislocation glides with kinks forming near the pining points ((i)-(ii) in Fig. 10b). After yielding, an inverse shear deformation was applied along the $1/3[\bar{2}11\bar{3}]$ direction to relax the remaining elastic strain to mimic the unloading process of the experiment indentation. It is found that the glided part of the dislocation gradually retracts to its original position during the unloading process ((ii)-(v) in Fig. 10b). Minimization of the elastic energy caused by dislocation line tension is thus suggested to be the driving force of the retraction. Interestingly, we also observe that the full retraction of the entire dislocation to its original position can result from an inverse stress that has a magnitude much smaller than the yield stress ((vi) in Fig. 10b). This implies that the residual stress emerged in the unloading process of the indentation experiment could cause dislocation retraction. It should be noted that the difference in time and length scale between MD simulation and experiments is large. Accordingly, the MD simulation here only intends to qualitatively provide a possible explanation to the experimental observation. Further studies at the mesoscale using the approaches like dislocation dynamic simulation are needed for a more quantitative analysis in the future.

4. Conclusions

In summary, we performed *in situ* TEM and MD simulations to reveal real-time dislocation and twinning activities in pure Mg during loading and unloading. The key observations can be listed as follows. (1) During loading, the screw component of $\langle \boldsymbol{c} + \boldsymbol{a} \rangle$ dislocations glide continuously, while the edge components rapidly become sessile. The twin tip propagation is intermittent, whereas the twin boundary migration is more continuous. (2) During unloading, both $\langle \boldsymbol{c} + \boldsymbol{a} \rangle$ dislocation retraction and detwinning were observed, which is likely driven by the residual stress and relaxation of the elastic strain. (3) The plastic zone comprised of $\langle \boldsymbol{c} + \boldsymbol{a} \rangle$ dislocations in Mg is well defined, which contrasts with the diffused plastic zones observed in FCC metals under the nanoindentation impressions. (4) The I_1 SFs bounded with a $\langle 1/2\boldsymbol{c}+\boldsymbol{p} \rangle$ Frank loop can form at an early stage of indentation and serve as a nucleation source for the abundant $\langle \boldsymbol{c} + \boldsymbol{a} \rangle$ dislocations observed experimentally.

Declaration of Competing Interest

All authors declared that there are no conflicts of interest.

Acknowledgments

This material is based upon work supported by the National Science Foundation (Division of Materials Research, Program Manager: Dr. Jonathan Madison) under Grant No. 2144973. The simulation work is financially supported by the startup fund from Drexel University. The authors would like to thank Dr. Wilson Serem for his support of the *in situ* TEM experiments. The use of the facility in the Microscopy Imaging Center and Materials Characterization Facility at Texas A&M University is also acknowledged. The computational resources at Drexel's University Research Computing Facility (Picotte) are also acknowledged.

Supplementary materials

Supplementary material associated with this article can be found, in the online version, at doi:10.1016/j.jma.2023.08.013.

References

[1] A.A. Luo, A.K. Sachdev, D. Apelian, J. Mater. Process. Technol. 306 (2022) 117606.
[2] A.A. Luo, JOM 54 (2) (2002) 42–48.
[3] A.A. Luo, R. Shi, J. Miao, T. Avey, JOM 73 (5) (2021) 1403–1418.
[4] S.R. Agnew, Ö. Duygulu, Int. J. Plast. 21 (6) (2005) 1161–1193.
[5] J. Zhang, S.P. Joshi, J. Mech. Phys. Solids 60 (5) (2012) 945–972.
[6] M. Barnett, Mater. Sci. Eng. A 464 (1–2) (2007) 1–7.
[7] T. Obara, H. Yoshinga, S. Morozumi, Acta Metall. 21 (7) (1973) 845–853.
[8] S.R. Agnew, J.A. Horton, M.H. Yoo, Metall. Mater. Trans. A 33 (3) (2002) 851–858.
[9] K.Y. Xie, Z. Alam, A. Caffee, K.J. Hemker, Scr. Mater. 112 (2016) 75–78.
[10] Y. Tang, J.A. El-Awady, Acta Mater. 71 (2014) 319–332.
[11] S.G. Hong, S.H. Park, C.S. Lee, Acta Mater. 58 (18) (2010) 5873–5885.
[12] Z. Wu, W.A. Curtin, Nature 526 (7571) (2015) 62–67.
[13] Z. Wu, W.A. Curtin, Scr. Mater. 116 (2016) 104–107.
[14] S. Sandlöbes, S. Zaefferer, I. Schestakow, S. Yi, R. Gonzalez-Martinez, Acta Mater. 59 (2) (2011) 429–439.
[15] B. Syed, J. Geng, R.K. Mishra, K.S. Kumar, Scr. Mater. 67 (7) (2012) 700–703.
[16] J. Geng, M.F. Chisholm, R.K. Mishra, K.S. Kumar, Philos. Mag. Lett. 94 (6) (2014) 377–386.
[17] J. Geng, M.F. Chisholm, R.K. Mishra, K.S. Kumar, Philos. Mag. 95 (35) (2015) 3910–3932.
[18] Z. Wu, W.A. Curtin, Proc. Natl. Acad. Sci. USA 113 (40) (2016) 11137–11142.
[19] Z. Ding, W. Liu, H. Sun, S. Li, D. Zhang, Y. Zhao, E.J. Lavernia, Y. Zhu, Acta Mater. 146 (2018) 265–272.
[20] K.Y. Xie, K.M. Reddy, L. Ma, A. Caffee, M. Chen, K.J. Hemker, Materialia 8 (2019) 100504.
[21] I. Beyerlein, L. Capolungo, P. Marshall, R. McCabe, C. Tomé, Philos. Mag. 90 (16) (2010) 2161–2190.
[22] N. Dixit, K.Y. Xie, K.J. Hemker, K. Ramesh, Acta Mater. 87 (2015) 56–67.
[23] D. Zhao, J. Dong, K.Y. Xie, MRS Commun. 12 (2) (2022) 217–222.
[24] H. El Kadiri, C.D. Barrett, J. Wang, C.N. Tomé, Acta Mater. 85 (2015) 354–361.
[25] A. Serra, D.J. Bacon, R.C. Pond, Phys. Rev. Lett. 104 (2) (2010) 029603.
[26] B. Li, E. Ma, Phys. Rev. Lett. 103 (3) (2009) 035503.

Please cite this article as: Y.-C. Lai, Y. Ying, D. Yadav et al., In situ TEM observations and molecular dynamics simulations of deformation defect activities in Mg via nanoindentation, Journal of Magnesium and Alloys, https://doi.org/10.1016/j.jma.2023.08.013

[27] K.Y. Xie, K. Hazeli, N. Dixit, L. Ma, K.T. Ramesh, K.J. Hemker, Sci. Adv. 7 (42) (2021) eabg3443.
[28] B.Y. Liu, J. Wang, B. Li, L. Lu, X.Y. Zhang, Z.W. Shan, J. Li, C.L. Jia, J. Sun, E. Ma, Nat. Commun. 5 (2014) 3297.
[29] L. Wu, A. Jain, D.W. Brown, G.M. Stoica, S.R. Agnew, B. Clausen, D.E. Fielden, P.K. Liaw, Acta Mater. 56 (4) (2008) 688–695.
[30] J. Ye, R.K. Mishra, A.K. Sachdev, A.M. Minor, Scr. Mater. 64 (3) (2011) 292–295.
[31] Q. Yu, L. Qi, K. Chen, R.K. Mishra, J. Li, A.M. Minor, Nano Lett. 12 (2) (2012) 887–892.
[32] Q. Yu, L. Qi, R.K. Mishra, J. Li, A.M. Minor, Proc. Natl. Acad. Sci. 110 (33) (2013) 13289–13293.
[33] A. Khosravani, D.T. Fullwood, B.L. Adams, T.M. Rampton, M.P. Miles, R.K. Mishra, Acta Mater. 100 (2015) 202–214.
[34] B.L. Wu, G.S. Duan, X.H. Du, L.H. Song, Y.D. Zhang, M.J. Philippe, C. Esling, Mater. Des. 132 (2017) 57–65.
[35] L. Jiang, M.A. Kumar, I.J. Beyerlein, X. Wang, D. Zhang, C. Wu, C. Cooper, T.J. Rupert, S. Mahajan, E.J. Lavernia, J.M. Schoenung, Mater. Sci. Eng. A 759 (2019) 142–153.
[36] B.Y. Liu, K.E. Prasad, N. Yang, F. Liu, Z.W. Shan, Acta Mater. 179 (2019) 414–423.
[37] D. Zhang, L. Jiang, X. Wang, I.J. Beyerlein, A.M. Minor, J.M. Schoenung, S. Mahajan, E.J. Lavernia, J. Mater. Res. 34 (9) (2019) 1499–1508.
[38] X. Wang, P. Mao, Z. Liu, Z. Wang, F. Wang, L. Zhou, Z. Wei, J. Alloys Compd. 817 (2020) 152967.
[39] C.L. Williams, C. Kale, S.A. Turnage, L.S. Shannahan, B. Li, K.N. Solanki, R. Becker, T.C. Hufnagel, K.T. Ramesh, Phys. Rev. Mater. 4 (8) (2020) 083603.
[40] B.Y. Liu, F. Liu, N. Yang, X.B. Zhai, L. Zhang, Y. Yang, B. Li, J. Li, E. Ma, J.F. Nie, Science 365 (6448) (2019) 73–75.
[41] B.Y. Liu, L. Wan, J. Wang, E. Ma, Z..W. Shan, Scr. Mater. 100 (2015) 86–89.
[42] D. Zhao, X. Ma, A. Srivastava, G. Turner, I. Karaman, K.Y. Xie, Acta Mater. 207 (2021) 116691.
[43] S. Plimpton, J. Comput. Phys. 117 (1) (1995) 1–19.
[44] D.Y. Sun, M.I. Mendelev, C.A. Becker, K. Kudin, T. Haxhimali, M. Asta, J.J. Hoyt, A. Karma, D.J. Srolovitz, Phys. Rev. B 73 (2) (2006) 024116.
[45] W.C.D. Cheong, L.C. Zhang, H. Tanaka, Key Eng. Mater. (2009) 31–42.
[46] A. Stukowski, Model. Simul. Mater. Sci. Eng. 18 (1) (2009) 015012.
[47] P. Hirel, Comput. Phys. Commun. 197 (2015) 212–219.
[48] X. Huang, Y.J. Hu, Q. An, J. Phys. Chem. C 125 (44) (2021) 24710–24718.
[49] H. Bei, E.P. George, J.L. Hay, G.M. Pharr, Phys. Rev. Lett. 95 (4) (2005) 045501.
[50] P.S. Phani, W. Oliver, Mater. Des. 164 (2019) 107563.
[51] H. Fan, J.A. El-Awady, J. Appl. Mech. 82 (10) (2015).
[52] F. Csikor Ferenc, C. Motz, D. Weygand, M. Zaiser, S. Zapperi, Science 318 (5848) (2007) 251–254.
[53] D. Catoor, Y.F. Gao, J. Geng, M.J.N.V. Prasad, E.G. Herbert, K.S. Kumar, G.M. Pharr, E.P. George, Acta Mater. 61 (8) (2013) 2953–2965.
[54] X. Ma, W. Higgins, Z. Liang, D. Zhao, G.M. Pharr, K.Y. Xie, Proc. Natl. Acad. Sci. 118 (30) (2021) e2025657118.
[55] K. Raineesh, K.E. Prasad, J. Mater. Res. 37 (3) (2022) 728–736.
[56] W.D. Nix, H. Gao, J. Mech. Phys. Solids 46 (3) (1998) 411–425.
[57] I.A. Alhafez, C.J. Ruestes, Y. Gao, H.M. Urbassek, Nanotechnology 27 (4) (2015) 045706.
[58] S. Jiao, W. Tu, P. Zhang, W. Zhang, L. Qin, Z. Sun, J. Chen, Comput. Mater. Sci. 143 (2018) 384–390.
[59] R. Kositski, D. Mordehai, Acta Mater. 90 (2015) 370–379.
[60] Z. Wu, R. Ahmad, B. Yin, S. Sandlöbes, W.A. Curtin, Science 359 (6374) (2018) 447–452.
[61] S.R. Agnew, L. Capolungo, C.A. Calhoun, Acta Mater. 82 (2015) 255–265.
[62] Z. Pei, J. Yin, Mater. Des. 186 (2020) 108286.
[63] S. Yoshikawa, D. Matsunaka, Comput. Mater. Sci. 179 (2020) 109644.
[64] K. Matsubara, H. Kimizuka, S. Ogata, Comput. Mater. Sci. 122 (2016) 314–321.
[65] A. Berghezan, A. Fourdeux, S. Amelinckx, Acta Metall. 9 (5) (1961) 464–490.
[66] Y.J. Hu, V. Menon, L. Qi, J. Magnes. Alloys 10 (10) (2022) 2717–2729.
[67] C. He, Y. Zhang, C.Q. Liu, Y. Yue, H.W. Chen, J.F. Nie, Acta Mater. 188 (2020) 328–343.
[68] Q. Qin, S. Yin, G. Cheng, X. Li, T.H. Chang, G. Richter, Y. Zhu, H. Gao, Nat. Commun. 6 (1) (2015) 5983.
[69] G. Cheng, S. Yin, C. Li, T.H. Chang, G. Richter, H. Gao, Y. Zhu, Acta Mater. 196 (2020) 304–312.
[70] H. Xiang, W. Guo, Sci. China Phys. Mech. Astron. 64 (6) (2021) 264611.
[71] H. Xiang, W. Guo, Int. J. Plast. 150 (2022) 103197.

Please cite this article as: Y.-C. Lai, Y. Ying, D. Yadav et al., In situ TEM observations and molecular dynamics simulations of deformation defect activities in Mg via nanoindentation, Journal of Magnesium and Alloys, https://doi.org/10.1016/j.jma.2023.08.013